

Precision measurement of the local bias of dark matter halos

Titouan Lazeyras,^a Christian Wagner,^{a,b} Tobias Baldauf,^c
Fabian Schmidt^a

^aMax-Planck-Institut für Astrophysik, Karl-Schwarzschild-Str. 1, 85748 Garching, Germany

^bLeibniz-Institut für Astrophysik, An der Sternwarte 16, 14482 Potsdam, Germany

^cInstitute for Advanced Study, Einstein Drive, Princeton, NJ 08540, United States

E-mail: titouan@mpa-garching.mpg.de, cwagner@mpa-garching.mpg.de,
t.baldauf@tbaweb.de, fabians@mpa-garching.mpg.de

Abstract. We present accurate measurements of the linear, quadratic, and cubic local bias of dark matter halos, using curved “separate universe” N-body simulations which effectively incorporate an infinite-wavelength overdensity. This can be seen as an exact implementation of the peak-background split argument. We compare the results with the linear and quadratic bias measured from the halo-matter power spectrum and bispectrum, and find good agreement. On the other hand, the standard peak-background split applied to the Sheth & Tormen (1999) and Tinker et al. (2008) halo mass functions matches the measured linear bias parameter only at the level of 10%. The prediction from the excursion set-peaks approach performs much better, which can be attributed to the stochastic moving barrier employed in the excursion set-peaks prediction. We also provide convenient fitting formulas for the nonlinear bias parameters $b_2(b_1)$ and $b_3(b_1)$, which work well over a range of redshifts.

Keywords: galaxy clustering, power spectrum, dark matter simulations, cluster counts

Contents

1	Introduction	1
2	Theory predictions	3
2.1	Peak-background split bias	3
2.2	Excursion set peaks	4
3	Bias parameters from separate universe simulations	4
3.1	Halo catalogs	5
3.2	Eulerian biases	6
4	Bias parameters from correlations	7
5	Results	9
5.1	Linear bias	9
5.2	Higher order biases	11
6	Conclusions	13
A	Halo bias from excursion set peaks	15
B	Comparison of Lagrangian and Eulerian separate universe biases	17
C	Effect of the degree of the fitting polynomial on the bias parameters	18
D	Fourth order bias	18
E	Covariance between the bias parameters	20

1 Introduction

The large-scale distribution of dark matter halos is one of the key ingredients of the theoretical description of large-scale structure (LSS). Since most observed tracers of LSS, such as galaxies, reside in halos, the statistics of halos determine those of galaxies on large scales. Similarly, the halo model description of the nonlinear matter density field [1] crucially relies on halo statistics. In the context of perturbation theory, the statistics of halos are written in terms of bias parameters multiplying operators constructed out of the matter density field. In general, these operators consist of powers of the matter density and tidal field [2, 3], as well as convective time derivatives of these quantities [4, 5]. However, the most well-studied and phenomenologically most important bias parameters on large scales are those multiplying powers of the matter density field, i.e.

$$\delta_h(\mathbf{x}, \tau) \supset b_1(\tau)\delta_\rho(\mathbf{x}, \tau) + \frac{1}{2}b_2(\tau)\delta_\rho^2(\mathbf{x}, \tau) + \frac{1}{6}b_3(\tau)\delta_\rho^3(\mathbf{x}, \tau) + \dots, \quad (1.1)$$

where δ_h is the fractional number density perturbation of a given halo sample, while δ_ρ is the matter density perturbation. More precisely, the powers of δ_ρ should be understood as renormalized operators [6–8]. The b_n are commonly called (nonlinear) *local bias parameters*. The

goal of this paper is to present precision measurements of b_1 , b_2 , b_3 using a novel technique, *separate universe simulations*.

In the separate universe approach [9–13], a long-wavelength density perturbation is included in an N-body simulation by changing the cosmological parameters, in particular Ω_m , Ω_Λ , Ω_K and H_0 , from their fiducial values, and running the simulation to a different scale factor. As argued in [8, 14, 15], the (renormalized) local bias parameters defined in Eq. (1.1) correspond to the response of the halo abundance, \bar{n}_h , to a long-wavelength density perturbation, equivalent to a change in the background density, $\bar{\rho}$,

$$b_n = \frac{\bar{\rho}^n}{\bar{n}_h} \frac{\partial^n \bar{n}_h}{\partial \bar{\rho}^n}. \quad (1.2)$$

This can be understood as an exact formulation of the peak-background split (PBS) [16, 17]. Thus, the b_n can be measured through the mass function of halos in a suite of separate universe simulations. This technique has several advantages: first, it is guaranteed to recover the large-scale limit of the b_n , without scale-dependent or nonlinear corrections which affect measurements of the bias parameters from the halo power spectrum and bispectrum, or from the cross-correlation with smoothed fields. Note that, starting at second order, “nonlocal” bias parameters such as those with respect to powers of the tidal field will enter in these latter measurements at the same level as the b_n . Second, we can straightforwardly obtain measurements of higher order bias parameters such as b_3 , which become cumbersome to measure using correlations. Finally, by using the same initial phases for simulations with different density, we can cancel to a large extent the cosmic variance contribution to the measurement error.

Separate universe simulations are expected to estimate the same set of bias parameters as those obtained from matter-halo cross-correlations. We will thus compare the biases obtained from the separate universe simulations to those determined by fitting to halo two- and three-point statistics. We also compare the results to biases derived from universal mass functions using the classic peak-background split argument, and recent theoretical predictions from the excursion set-peaks (ESP) approach [18, 19], which incorporates some aspects of the Gaussian peaks model into the excursion set framework.

Higher order bias parameters have previously been measured in simulations by correlating the halo number with powers of the smoothed density field at the final time (Eulerian frame) [20, 21] or in the initial conditions [22]. However, the bias parameters measured in this way depend on the smoothing scale adopted, while the local bias parameters that are relevant for perturbation theory predictions, and that we are interested in here, correspond to a smoothing scale of infinity. Further, all these references neglect the nonlocal bias terms mentioned above, which will affect the inferred values of b_2 and higher. For these reasons, it is difficult to directly compare our measurements of nonlinear bias parameters with these previous results (although we find broad agreement). We stress again that in the separate universe approach we are guaranteed to obtain the local bias in the large-scale limit, without nonlinear or tidal corrections. Moreover, we simultaneously obtain both the Eulerian (b_n) and Lagrangian (b_n^L) bias parameters.

Two related papers appeared on the preprint archive simultaneously to this paper. Ref. [23] measured the linear bias using separate universe simulations through an abundance matching technique which yields the integrated halo bias above a mass threshold. This technique reduces the shot noise in the bias measurement. Ref. [24] also measured the linear bias via the mass function. In addition, they present measurements of b_2 through the response

of the halo power spectrum to a long-wavelength mode (as done in [12, 25] for the matter power spectrum). Our results are consistent with the findings of both of these references. However, unlike these and any other previous published results, we use the fully nonlinear separate universe approach to obtain accurate measurements of the *linear and nonlinear* local biases.

In this paper we adopt a flat Λ CDM fiducial cosmology with $\Omega_m = 0.27$, $h = 0.7$, $\Omega_b h^2 = 0.023$ and $\mathcal{A}_s = 2.2 \cdot 10^{-9}$. The outline of the paper is as follows. In section 2, we present the theoretical predictions that we will compare our measurements with. Section 3 describes the technique of measuring bias parameters from separate universe simulations, while section 4 presents the estimators for b_1 and b_2 using the conventional approach of measuring halo correlations. We discuss the results in section 5. We conclude in section 6. The appendices contain more details on the ESP predictions as well as our bias measurements.

2 Theory predictions

In this section we present several theoretical predictions for the large-scale bias from the literature. We first recap the PBS argument in section 2.1 and briefly present the ESP formalism in section 2.2.

Before jumping into details, we briefly explain the definitions of *Lagrangian* and *Eulerian* halo bias. The Lagrangian bias links the abundance of dark matter halos to the density perturbations in Lagrangian space, i.e. it describes the relation of proto-halos in the initial conditions that correspond to halos identified at redshift z to the initial linear density perturbation field. On the other hand, the Eulerian bias relates the halos identified at redshift z to the nonlinear density field, δ_ρ , at redshift z . In the case of the local bias parameters considered here, there is an exact nonlinear mapping between the Lagrangian bias parameters b_n^L and their Eulerian counterparts b_m , see Appendix B. We will make use of this mapping both for the theory predictions and measurements.

In the following, the top-hat filtered variance on a scale R_{TH} (the Lagrangian radius of halos) is denoted as

$$\sigma_0^2 \equiv \int d \ln k \Delta^2(k) [W_{\text{TH}}(kR_{\text{TH}})]^2, \quad (2.1)$$

where $\Delta^2(k) = k^3 P(k)/2\pi^2$ is the dimensionless linearly extrapolated matter power spectrum and the top-hat filter in Fourier space $W_{\text{TH}}(kR_{\text{TH}})$ is given in Eq. (A.1).

2.1 Peak-background split bias

We briefly recap how the bias parameters can be derived from the differential halo mass function using the PBS argument, as initially proposed in [16, 17, 26]. Following the PBS argument, the effect of a long wavelength mode δ_0 on the small scale formation can be seen as locally modulating the density threshold for halo formation, or barrier B , sending it to $B - \delta_0$ (here we denote the barrier as B to emphasize that this argument is not restricted to the constant spherical collapse threshold δ_c and can be extended to barriers depending e.g. on the halo mass M through σ_0). Note that, in the case where stochasticity should be introduced in the barrier, this shift does not modify the stochastic contribution to the barrier, which is supposed to capture the effect of small-scale modes. We define the differential mass function as

$$n(\nu_B) = \frac{\bar{\rho}_m}{M} f(\nu_B) \left| \frac{d \ln \sigma_0}{d \ln M} \right|, \quad (2.2)$$

with $\nu_B \equiv B(\sigma_0)/\sigma_0$ (we reserve the notation ν for $\nu \equiv \delta_c/\sigma_0$), M the corresponding mass and $f(\nu_B)$ the mass fraction contained in halos of mass M . The scale-independent large-scale Lagrangian bias parameters are then defined by the well known relation

$$b_n^L(\nu_B) = \frac{1}{n(\nu_B)} \left. \frac{\partial^n n([B(\sigma_0) - \delta_0]/\sigma_0)}{\partial \delta_0^n} \right|_{\delta_0=0}. \quad (2.3)$$

As we have indicated, this also applies if the deterministic part of the barrier is mass-dependent. We will use Eq. (2.3) both to derive the bias in the ESP model and from the fits to the mass function proposed in [27] and [28] (hereafter ST99 and T08 respectively).

2.2 Excursion set peaks

In this section, we review the ESP formalism proposed in [18] and [19]. The details of the calculation are relegated to Appendix A. All the results that we present here and in Appendix A were already derived in these two references, but in a different way; here, we use the PBS argument to derive the bias parameters directly. Further, the ESP predictions for b_3 and b_4 are computed here for the first time.

The ESP aims at unifying the peak model of Bardeen et al. in 1986 (hereafter BBKS) [29] and the excursion set formalism of Bond et al. in 1991 [30]. It can be seen either as addressing the cloud-in-cloud problem within the peak model, or as applying the excursion set formalism to a special subset of all possible positions (the peaks). We follow [19], who chose a top-hat filter for the excursion set part, and a Gaussian filter to identify peaks (in order to ensure finite moments of derivatives of the smoothed density field).

More importantly, [19] improved the model by adding a mass-dependent stochastic scatter to the threshold. Specifically, the barrier is defined as [18]

$$B(\sigma_0) = \delta_c + \beta\sigma_0. \quad (2.4)$$

Here, β is a stochastic variable and [19] chose its PDF $p(\beta)$ to be lognormal with mean and variance corresponding to $\langle\beta\rangle = 0.5$ and $\text{Var}(\beta) = 0.25$. This choice was made to match the peak height measured in simulations by [31]. Hence β takes only positive values. Note that Eq. (2.4) then corresponds to a mass-dependent mean barrier $\delta_c + 0.5\sigma_0$.

As we show in Appendix A, the Lagrangian bias parameters in the ESP can be directly derived from Eq. (2.3) by inserting the multiplicity function $f_{\text{ESP}}(\nu)$ into Eq. (2.2), and sending $\nu = \delta_c/\sigma_0$ to $\nu_1 = \nu(1 - \delta_0/\delta_c)$.¹ Our results for the bias, Eq. (A.14), are identical to the large-scale bias parameters derived using a different approach in [18, 19]. We will see that the choice of barrier Eq. (2.4) leads to significant differences from the standard PBS biases derived using $B = \delta_c$ from the T08 and ST99 mass functions.

3 Bias parameters from separate universe simulations

Our results are based on the suite of separate universe simulations described in [13, 25], performed using the cosmological code GADGET-2 [32]. The idea of the separate universe simulations is that a uniform matter overdensity δ_ρ of a scale larger than the simulation box can be absorbed in the background density $\tilde{\rho}_m$ of a modified cosmology simulation

¹Here one needs to take care not to shift one instance of ν in the expression for $f_{\text{ESP}}(\nu)$ that is actually unrelated to the barrier. See Appendix A.

(throughout the whole paper, quantities in modified cosmologies will be denoted with a tilde), where

$$\tilde{\rho}_m(t) = \rho_m(t) [1 + \delta_\rho(t)], \quad (3.1)$$

with ρ_m the mean matter density in a simulation with no overdensity (which we call the fiducial cosmology). Indeed, a uniform density can only be included in this way, since the Poisson equation for the potential enforces a vanishing mean density perturbation over the entire box. Thus one can see a simulation with a constant overdensity δ_ρ as a separate universe simulation with a properly modified cosmology. Qualitatively, a positive overdensity causes slower expansion and enhances the growth of structure, i.e. more halos, whereas a negative one will have the opposite effect. The precise mapping of δ_ρ to modified cosmological parameters is described in [13]. Crucially, we work to fully nonlinear order in $\delta_\rho(t)$.

We use two sets of simulations denoted by “lowres” and “highres” throughout the paper. Both have a comoving box size of $500 h^{-1}\text{Mpc}$ in the fiducial cosmology. The “lowres” set uses 256^3 particles in each simulation, while “highres” employs 512^3 particles. For both sets, we run the fiducial cosmology, i.e. $\delta_\rho = 0$, and simulations with values of δ_ρ corresponding to $\delta_L = \{\pm 0.5, \pm 0.4, \pm 0.3, \pm 0.2, \pm 0.1, \pm 0.07, \pm 0.05, \pm 0.02, \pm 0.01\}$, where δ_L is the present-day linearly extrapolated matter density contrast. In addition, we simulate separate universe cosmologies corresponding to $\delta_L = 0.15, 0.25, \text{ and } 0.35$ for both resolutions. This makes the sampling in the final, nonlinear δ_ρ more symmetric around 0 which should help diminish the covariance between the bias parameters.² The comoving box size in the modified cosmology simulations is adjusted to match that in the fiducial cosmology, $L = 500 h^{-1}\text{Mpc}$. Hence, in the high redshift limit ($z \rightarrow \infty$ for which $\delta_\rho \rightarrow 0$) the physical size of the box is the same for all simulations whereas at the present time ($z = 0$ in the fiducial cosmology) the physical size of the simulation box varies with δ_ρ . However, this choice of the box size has the advantage that the physical mass resolution is the same within each set of simulations regardless of the simulated overdensity δ_ρ (i.e. $\tilde{m}_p = m_p$ where m_p is the particle mass in the fiducial cosmology). Since the biases are determined by comparing halo abundances between different overdensities, this eliminates any possible systematic effects in the biases due to varying mass resolution. The mass resolution is $m_p = 5.6 \cdot 10^{11} h^{-1} M_\odot$ in the “lowres” set of simulations and $m_p = 7 \cdot 10^{10} h^{-1} M_\odot$ in the “highres” one. Furthermore, for the “lowres” set of simulation, we ran 64 realizations of the entire set of δ_L values. For the “highres” one we ran only 16 realizations of each δ_L value as they are more costly in terms of computation time. Each simulation was initialized using 2LPT at $z_i = 49$. For further details about the simulations, see [25].

3.1 Halo catalogs

The halos were identified using the Amiga Halo Finder (hereafter AHF) [33, 34], which identifies halos with a spherical overdensity (SO) algorithm. We identify halos at a fixed proper time corresponding to $z = 0$ in the fiducial cosmology. In this paper, we only use the number of distinct halos and do not consider their sub-halos.

The key point in identifying halos with the spherical overdensity criterion is the setting of the density threshold. We choose here a value of $\Delta_{\text{SO}} = 200$ times the background matter density in the *fiducial* cosmology. Thus, our measured bias parameters are valid for this

²We have not performed a systematic study on the number of δ_L values that are necessary to derive accurate measurements of the b_n up to a given order. Given the significant degeneracies between b_n and b_{n+2} we have found (Appendix E), this is a nontrivial question.

specific halo definition. For the simulations with a different background density, the threshold must be rescaled in order to compare halos identified using the same physical density in each simulation. Specifically, we need to use

$$\Delta_{\text{so}} = \frac{200}{1 + \delta_\rho}. \quad (3.2)$$

Another point is the treatment of the particle unbinding in a halo. AHF has the ability to remove unbound particles, i.e particles which are not gravitationally bound to the halo they are located in. However, in order to avoid having to implement the complicated matching of the unbinding criterion between the modified and fiducial cosmologies, we have turned unbinding off in all halo catalogs. Note that the effect of unbinding is very small (of order 1% on the mass function), and that we consistently use the same halo catalogs for all measurements, so that this choice does not affect our comparison between different methods for measuring bias.

We count halos in top-hat bins given by

$$W_n(M, M_{\text{center}}) = \begin{cases} 1 & \text{if } |\log_{10}(M) - \log_{10}(M_{\text{center}})| \leq 0.1 \\ 0 & \text{otherwise,} \end{cases} \quad (3.3)$$

where M is the mass (M_{center} corresponding to center of the bin). For the high resolution simulations, we count halos in 12 bins centered from $\log_{10}(M_{\text{center}}) = 12.55$ to $\log_{10}(M_{\text{center}}) = 14.75$, to ensure that we have enough halos in each bin. For the low resolution simulations, we have 7 bins from $\log_{10}(M_{\text{center}}) = 13.55$ to $\log_{10}(M_{\text{center}}) = 14.75$. With this binning choice, the lowest bin is centered around halos with 63 particles for the “lowres” set of simulations, with a lower limit at halos containing around 50 particles. For the “highres” set of simulations, the lowest mass bin is centered on halos with around 51 particles, with a lower limit around 40 particles. These numbers are quite low compared to more conservative values (e.g. 400 particles in T08). However δ_h is the *relative difference* of the number of halos between the fiducial and modified cosmology simulations (see Eq. (3.4) hereafter) and therefore that quantity should be less affected by resolution effects. For halos with a minimum number of 40 particles, we did not find any systematic difference between the bias parameters measured from the “lowres” and “highres” simulations. Thus, we present results for halos that are resolved by at least 40 particles.

3.2 Eulerian biases

Instead of fitting the Eulerian bias parameters directly to the simulation results, we derive them from the measured Lagrangian biases for which the fitting is more robust, using the exact nonlinear evolution of δ_ρ (see Appendix B for the details of the mapping). In order to obtain the Lagrangian bias parameters, we compute $\delta_h(M, \delta_L)$ versus δ_L where $\delta_h(M, \delta_L)$ is the overdensity of halos in a bin of mass M compared to the fiducial case $\delta_L = 0$,

$$\delta_h(M, \delta_L) = \frac{\tilde{N}(M, \delta_L) - N(M)}{N(M)}, \quad (3.4)$$

with $\tilde{N}(M, \delta_L)$ the number of halos in a bin centered around mass M in the presence of the linear overdensity δ_L and $N(M) = \tilde{N}(M, \delta_L = 0)$. Note that $\delta_h(M, \delta_L)$ is the overdensity of halos in Lagrangian space as the physical volumes of the separate universe simulations only coincide at high redshift.

In order to obtain the Lagrangian bias parameters b_n^L , we then fit Eq. (3.4) by

$$\delta_h = \sum_{n=1}^5 \frac{1}{n!} b_n^L (\delta_L)^n. \quad (3.5)$$

As indicated in Eq. (3.5) we use a 5th order polynomial in δ_L by default. In Appendix C we study the effect of the degree of the polynomial on the results; as a rough rule, if one is interested in b_n^L , then one should fit a polynomial up to order $n + 2$.

In order to estimate the overall best-fit of and error bars on the bias parameters, we use a bootstrap technique. For each non zero δ_L value, we randomly produce p resamples of the mass function. Each resample is composed of the same number of realizations as the original sample (i.e. 16 or 64) and we choose $p = 100 \cdot 64$ ($100 \cdot 16$) for the low (high) resolution simulations. We then compute the average number of halos per mass bin for each resample. This gives us p numbers $\tilde{N}^i(M, \delta_L)$. For a given δ_L , we also create the same set of resamples for the fiducial cosmology and again compute the average number of halos, i.e. $N^i(M)$. We then compute p times δ_h^i according to Eq. (3.4) for every δ_L value. Since we use the same resamples for the separate universe results, $\tilde{N}^i(M, \delta_L)$, and the fiducial case, $N^i(M)$, the cosmic variance is canceled to leading order. The error on δ_h at fixed mass and δ_L is given by the sample variance and we use it as a weight for the fit. We neglect, however, the covariance between $\tilde{N}^i(M, \delta_L)$ for different δ_L values. We then produce p fits with a weighted least squares method. For every bias parameter, the value we report is the mean of the results of the p fits while the corresponding error bar is given by the square root of the variance of the distribution. Within the mass range common to both sets of simulations “lowres” and “highres”, the measurements are consistent with each other and hence we perform a volume-weighted average of the biases from the two sets of simulations.

4 Bias parameters from correlations

Traditionally bias parameters are used for and measured from n -point correlation functions or n -spectra. The n -th order bias parameters enter the tree-level calculation of the $n+1$ -point functions. For instance, b_1 appears at the leading order in the large-scale behavior of the halo power spectrum, b_2 in the large-scale limit of the bispectrum and b_3 in the large-scale limit of the trispectrum. For the comparison to n -point functions, we will restrict ourselves to the power spectrum and bispectrum at tree level here. The bispectrum also contains nonlocal bias parameters, i.e. biases with respect to the tidal field, that arise from triaxial collapse and gravitational evolution. The estimation of the first and second order bias parameters closely follows the steps outlined in [35] (see also [36]), with the difference that we are performing a joint fit for all the bias parameters, instead of first fitting b_1 to the halo power spectrum and then using its value in the bispectrum analysis.

Let us start by discussing the power spectrum. We measure the halo-matter cross power spectrum P_{hm} , which at tree level (on large scales) is given by

$$P_{\text{hm}}(k) = b_1 P_{\text{mm}}(k). \quad (4.1)$$

We refrain from explicitly including the loop corrections, since they contain third order biases not present in the bispectrum as well as scale-dependent biases $\propto k^2$ [7]. The advantage of the halo-matter cross power spectrum over the halo-halo power spectrum is that it is free of shot noise. To ensure that our measurements are not contaminated by higher order contributions

or scale dependent bias, we will in fact fit $P_{\text{hm}}(k) = (b_1 + b_{P,k^2}k^2)P_{\text{mm}}(k)$ to the simulation results, where b_{P,k^2} is a free nuisance parameter. This term absorbs the loop corrections in the large-scale limit. We measure the matter and halo power spectra in the same wavenumber bins in the simulation and take their ratio to cancel the leading cosmic variance, i.e. we define a quantity $q(k) = P_{\text{hm}}(k)/P_{\text{mm}}(k)$ and the χ^2

$$\chi_P^2 = \sum_k^{k_{\text{max}}} \left(\frac{q(k) - b_1 - b_{P,k^2}k^2}{\sigma[q(k)]} \right)^2, \quad (4.2)$$

where the variance $\sigma^2(q)$ is estimated from the box-to-box scatter between the simulation realizations.

Let us now turn to the bispectrum. One can form three different bispectra containing the halo field, the halo-halo-halo, the halo-halo-matter and the halo-matter-matter bispectrum. We are using the latter, since it is the only bispectrum free of shot noise. Furthermore, we will employ the unsymmetrized bispectrum, where the halo mode is the one associated with the wavevector \vec{k}_3 . This unsymmetrized bispectrum measurement allows for a clear distinction of the second order local bias b_2 and tidal tensor bias b_{s^2} , once the matter bispectrum is subtracted out. The unsymmetrized tree-level bispectrum reads

$$B_{\text{mmh}}(k_1, k_2, k_3) = b_1 B_{\text{mmm}}(k_1, k_2, k_3) + b_2 P(k_1)P(k_2) + 2b_{s^2} S_2(\vec{k}_1, \vec{k}_2) P(k_1)P(k_2), \quad (4.3)$$

where B_{mmm} is the tree-level matter bispectrum (e.g., [35]), and we employed the tidal operator S_2 defined as

$$S_2(\vec{k}_1, \vec{k}_2) = \left(\frac{\vec{k}_1 \cdot \vec{k}_2}{k_1^2 k_2^2} - \frac{1}{3} \right). \quad (4.4)$$

Similarly to the power spectrum defined above, this bispectrum does not include loop corrections or scale dependent biases. Thus, we again add a term of the form $b_{B,k^2}(k_1^2 + k_2^2)P(k_1)P(k_2)$ with a free coefficient b_{B,k^2} , designed to absorb the loop corrections. To cancel cosmic variance, we define the ratio of bispectrum and power spectrum measurements

$$Q(k_1, k_2, k_3; b_1) = \frac{B_{\text{mmh}}(k_1, k_2, k_3) - b_1 B_{\text{mmm}}(k_1, k_2, k_3)}{P_{\text{mm}}(k_1)P_{\text{mm}}(k_2)}, \quad (4.5)$$

and using this we define the corresponding χ^2

$$\chi_B^2 = \sum_{k_1, k_2, k_3}^{k_{\text{max}}} \left(\frac{Q(k_1, k_2, k_3; b_1) - b_2 - 2b_{s^2} S_2 - b_{B,k^2}(k_1^2 + k_2^2)}{\sigma[Q(k_1, k_2, k_3; b_{1,\text{fid}})]} \right)^2, \quad (4.6)$$

where the variance of Q is estimated from the box-to-box scatter between the simulation realizations for a fiducial $b_{1,\text{fid}}$. Equivalent results could have been obtained using the estimator presented in [37]. We decided to stick with the more traditional bispectrum estimation for the following reasons: for their method the smoothing scale of the fields needs to be chosen before the simulation data is reduced, complicating convergence tests. Furthermore, [37] ignored two-loop corrections to their estimator and higher derivative terms, while we marginalize over an effective shape accounting for the onset of scale dependence. A detailed comparison of the two methods is however beyond the scope of this work.

All measurements are done on the “lowres” and “highres” sets of the fiducial cosmology. We find the best fit biases b_1 and b_2 by sampling the log-likelihood $\ln \mathcal{L} = -\chi_{\text{tot}}^2/2$, where

$\chi_{\text{tot}}^2 = \chi_P^2 + \chi_B^2$ using the Markov Chain code EMCEE [38]. The errors on the bias parameters are estimated from the posterior distribution of sampling points after marginalizing over the (for our purposes) nuisance parameters b_{P,k^2} , b_{B,k^2} and b_s^2 . We have varied that maximum wavenumber k_{max} to ensure that we remain in the regime where the tree level bias parameters remain consistent with increasing k_{max} . Further, we demand that the total χ^2 per degree of freedom is approximately unity. The results shown below use a conservative value of $k_{\text{max}} = 0.06 h \text{Mpc}^{-1}$. This limits the number of modes to $\mathcal{O}(100)$ and thus also the number of power and bispectrum configurations. Due to the cancellation of the leading order cosmic variance this is not of major concern. We have compared the clustering constraints with a larger $2400 h^{-1} \text{Mpc}$ box providing a factor of 100 more modes to the same cutoff and found consistent results.

5 Results

This section presents the results for the Eulerian bias parameters b_1 to b_3 . For completeness, we also present results for b_4 , which is poorly constrained, in Appendix D.

In order to obtain a precise comparison between any theoretical prediction for the bias $b_n(M)$ (such as the ESP, Eq. (A.14)) and our data points, we convolve the theoretical prediction with the mass bins used in the simulation (see section 3). I.e., the theory predictions we will show in the following are given by

$$b_n^{\text{conv}}(M) = \frac{\int W_n(M', M) n(M') b_n(M') dM'}{\int W_n(M', M) n(M') dM'}, \quad (5.1)$$

where $W_n(M', M)$ is the window function of the mass bin given by Eq. (3.3), and $n(M')$ is the differential halo mass function, parametrized by the fitting formula of Eq. (2) in T08. In this way, we obtain smooth curves for the theory prediction whose value at the center of a given mass bin can be compared directly to the simulation results.

5.1 Linear bias

Figure 1 presents the results for b_1 . The green points show the results obtained from the separate universe simulations, while the red crosses show those from fitting P_{hm} and B_{mmh} . The mutual agreement of the two measurements is very good (the only point with relative difference greater than the 1σ uncertainty is at $\log M = 13.15$). The error bars of the separate universe measurements are significantly smaller. Note however that the effective volume used by these measurements is also larger, since the halo-matter power spectrum was only measured in the fiducial boxes. This is a first validation of the separate universe method and also proves its efficiency.

These results are consistent with the ones presented in [23] who derived the linear bias from abundance matching. Since Ref. [23] used a linearized implementation of separate universe simulations, they are restricted to small overdensities (they take $\delta_\rho = \pm 0.01$), resulting in very small changes in the halo abundance. For such small changes, abundance matching is much more efficient than binning halos into finite mass intervals. We circumvent this issue by using fully nonlinear separate universe simulations which allow us to simulate arbitrary values of δ_ρ .

We also compare our data with several results from the literature. The solid black curve is the fit to P_{hm} measurements from Tinker et al. (2010) [39] [their Eq. (6)]. As shown in the lower panel of Figure 1, the agreement is better than 5%, the quoted accuracy of the

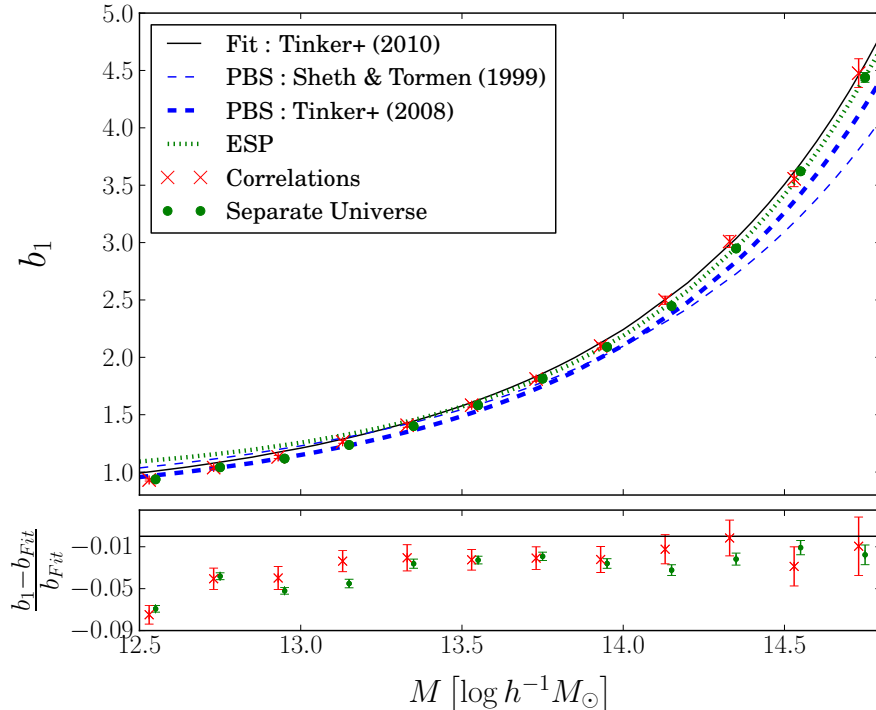


Figure 1: Top panel: comparison between the linear halo bias from separate universe simulations (green dots), and from clustering (red crosses; displaced slightly horizontally for clarity). Error bars that are not visible are within the marker size. The solid black curve is the Tinker et al. (2010) best fit curve for b_1 , while the dot-dashed green curve is the ESP prediction Eq. (A.14). We also show the result obtained by applying the PBS argument [Eq. (2.3)] to the T08 and ST99 mass functions (blue dashed curves). **Bottom panel:** relative difference between the measurements and the Tinker et al. (2010) best fit.

fitting formula. Note that we do not remove unbound particles from our halos, which we expect to lead to a slight underestimate of the bias at the few percent level at low masses. Next, we turn to the “standard” peak-background split argument Eq. (2.3) applied to the universal mass functions of ST99 and T08 (blue dashed curves). At low masses, the T08 curve is at 1% level agreement but the ST99 prediction overestimates the bias by around 8%. The agreement is worse at high mass where these two curves underestimate the bias by around 8% and 11% respectively.

The green dot-dashed line finally shows the prediction from excursion set peaks Eq. (A.14). The agreement at high masses is excellent, where the ESP matches the measured b_1 to better than 2%. The agreement is far less good at low masses where the ESP prediction overestimates the bias by roughly 10%. Note that the assumption that halos correspond to peaks in the initial density field is not expected to be accurate at low masses [40]. Part of the discrepancy might also come from the up-crossing criterion applied to derive the ESP prediction, which is only expected to be accurate at high masses [41]. It is worth emphasizing that Eq. (2.3) still applies in the case of the ESP. That is, the large-scale bias can still be derived directly from the mass function. The key difference to the PBS curves discussed previously is that, following [19], we employ a stochastic moving barrier, which changes the

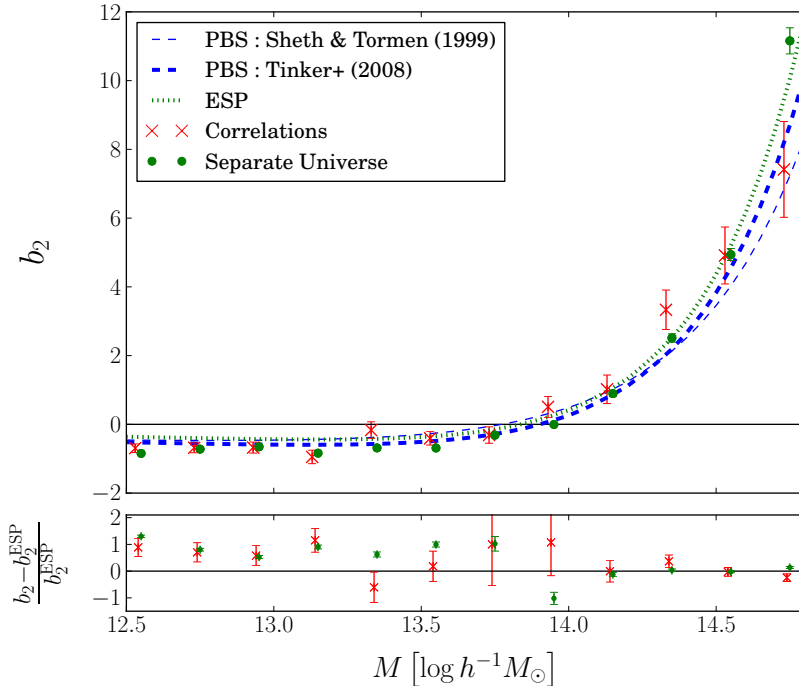


Figure 2: Top panel: same as Figure 1, but for the quadratic bias b_2 . The color code is as in Figure 1. **Bottom panel:** relative difference between measurements and the theoretical prediction of the ESP. In each panel, the clustering points have been horizontally displaced as in Figure 1.

relation between mass function and bias. This more realistic barrier leads to the significant improvement in the prediction of the bias for high-mass halos.

5.2 Higher order biases

Figures (2)–(3) present the analogous results of Figure 1 for b_2 and b_3 , respectively. For b_2 at masses below $10^{13.5} h^{-1} M_\odot$, there is some scatter in the separate universe results that is apparently larger than what is expected given the error bars (a hint of a similar effect can be seen in b_1 as well). Note however that there is significant residual degeneracy between the b_n for a given mass bin, so that a “ χ -by-eye” can be misleading. As an example, we show projections of the likelihood for one mass bin in Figure 8. The covariance between the bias parameters is further explored in Appendix E. Covariance in the halo shot noise between different mass bins, which we do not take into account in the likelihood, could also contribute to the fluctuations in the bias parameters.

In the case of b_2 , we can compare the separate universe results to the results of fitting to P_{hm} and B_{mmh} . Again, we find good agreement, with all points being within 2σ from each other. Note that b_2 is most difficult to constrain from correlations around its zero-crossing. The difference in constraining power between the two methods is now even larger than in the case of b_1 . This is because, when using correlations, b_2 has to be measured from a higher order statistic which has lower signal-to-noise. In the case of b_3 , a measurement from correlations would have to rely on the trispectrum and accurate subtraction of 1-loop contributions in perturbation theory. We defer this significantly more involved measurement to future work.

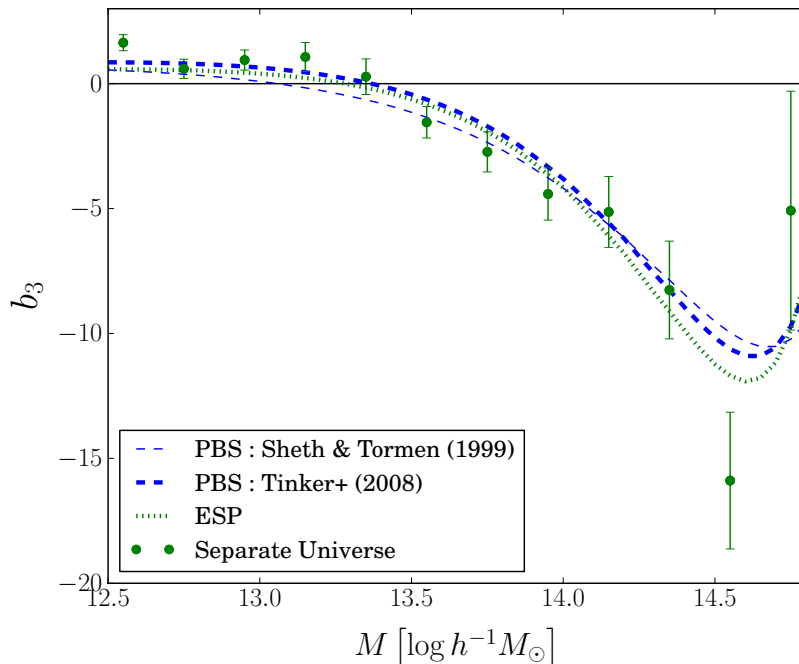


Figure 3: As Figure 2 but for b_3 .

As discussed in the introduction, it is difficult to rigorously compare these measurements to previously published results, since those were measured at a fixed smoothing scale and did not take into account nonlocal bias terms. Nevertheless, our results for b_2 and b_3 appear broadly consistent with those of [20, 22] and [20], respectively.

We again compare with the peak-background split results, now derived at second and third order from the ST99 and T08 mass functions. For b_2 , at low mass, both predictions deviate from our measurements by about 50%. At high mass, the deviation is at most 25% for T08 and 40% for ST99. In the low mass range, this apparently big discrepancy is also due to the smallness of the absolute value of b_2 . In the case of b_3 , the PBS predictions using either the T08 or ST99 mass functions are in fact completely consistent with the measurements at masses $\gtrsim 10^{12.7} h^{-1} M_\odot$ and $10^{13.5} h^{-1} M_\odot$, respectively.

Turning to the ESP prediction, we again find very good agreement at high masses, although for b_2 and b_3 the performance is not significantly better than the PBS-derived biases from the T08 mass function. At low masses, we again find larger discrepancies, with the ESP now underpredicting the magnitude of b_2 and b_3 . The same caveats regarding the relation of low-mass halos to peaks and the efficiency of the up-crossing condition apply here, i.e. we do not expect the ESP prediction to work well for those masses.

So far, we have only shown results at redshift 0. Figure 4 shows results from various redshifts by plotting b_2 , b_3 as functions of b_1 . If the bias parameters are uniquely determined by $\sigma_0 = \sigma(M)$, then this relation will be redshift-independent. Indeed, we find no evidence for a redshift dependence over the range $z = 0 \dots 2$ and $b_1 = 1 \dots 10$. Note that we have kept the overdensity criterion $\Delta_{S0} = 200$ fixed. Since the separate universe simulation measurements of b_2 and b_3 are very accurate, we provide fitting formulas in the form of

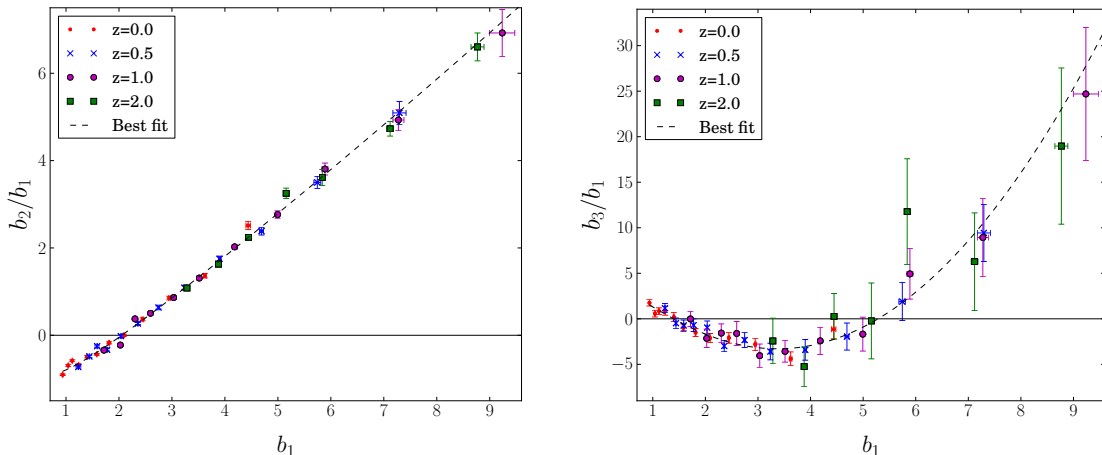


Figure 4: b_2 and b_3 as a function of b_1 obtained from separate universe simulations and for different redshifts. The dashed curves present the third order best fit polynomial for each bias. See text for details about the fit.

$b_n(b_1)$ for convenience. Given the consistency with a universal behavior, we perform a joint fit of results from all redshifts. We use a 3rd order polynomial form for both b_2 and b_3 . Again, we use a weighted least squares method for the fit but do not take into account the error on b_1 since it is much smaller than those in b_2 , b_3 . We obtain

$$b_2(b_1) = 0.412 - 2.143 b_1 + 0.929 b_1^2 + 0.008 b_1^3, \quad (5.2)$$

and

$$b_3(b_1) = -1.028 + 7.646 b_1 - 6.227 b_1^2 + 0.912 b_1^3. \quad (5.3)$$

The fits are shown as dashed lines in the two panels of Figure 4. Notice that we restricted ourselves to $b_1 < 9.6$ on these figures for clarity but we used the full range of results to produce the fits. Note that one should be careful when using these formulas outside the fitting range $1 \lesssim b_1 \lesssim 10$. Eqs. (5.2)–(5.3) are similar to the fitting formulas provided in [42] who fitted 2nd and 3rd order polynomials for $b_2(b_1)$ and $b_3(b_1)$, respectively, to PBS predictions, and found no redshift dependence of their results. Such universal relations became already apparent in [36] (their figure 9).

6 Conclusions

We have presented a new method to measure the large-scale, renormalized local density bias parameters b_n of dark matter halos, with $n = 1, 2, 3$, by running simulations which simulate an infinite-wavelength density perturbation of arbitrary amplitude. This method can be seen as an exact implementation of the peak-background split. This method has several advantages, including a simple implementation applicable, in principle, to arbitrarily high n . The most important advantage, however, is that the measured biases are not affected by the modeling of scale-dependent or nonlinear corrections, and there is no ambiguous choice of k_{max} , with the associated risk of overfitting, as when fitting halo N -point functions. The most significant disadvantage of the method is that it needs a set of dedicated simulations

with varying cosmological parameters to generate a range of δ_L (note however that once the simulations are done, they can be used for various studies, such as for example the nonlinear power spectrum response [25]).

We have compared our results for b_1 and b_2 to those measured from the halo-matter power spectrum and halo-matter-matter bispectrum, and find excellent agreement overall. One necessary condition for this agreement is a careful fitting procedure of the halo statistics and choice of k_{\max} .

We also compared our results to predictions based on the analytical peak-background split. Once a specific barrier B is assumed, the PBS allows for a derivation of all local bias parameters b_n from a given halo mass function. The simplest and most common choice is $B = \delta_c$, which we have applied to the ST99 and T08 mass function prescriptions. We found that even though the latter provides a very accurate mass function, the linear bias derived via the PBS and simple collapse threshold is only accurate at the $\sim 10\%$ level, in agreement with previous results [43]. Things are even worse for b_2 , with up to 50% discrepancy at low mass, although the absolute difference between the PBS predictions and the measurements is similar to that in b_1 . For b_3 , the simple PBS predictions are consistent with the measurements (at least at high masses), but this is not a very strong statement given the large error bars on b_3 .

We also derived the biases predicted in the excursion set-peaks approach, which includes a stochastic moving barrier motivated by simulation results. At high mass, this performs much better, at least for b_1 , showing that the choice of barrier is a key ingredient in deriving accurate bias parameters. In this context, it is important to note that previous results on the inaccuracy of PBS bias parameters [43] relied on the simple constant threshold $B = \delta_c$. This shows that the cause of these inaccuracies is not the peak-background split itself. The inaccuracy of the peak-background split thus depends on what one defines PBS to mean, and can be summarized as follows:

- The PBS implemented via the separate universe approach is exact.
- The PBS using a simulation-derived stochastic moving barrier [19, 31], as in the ESP, is accurate to a few percent, at least at high masses. The discrepancy found at low mass can be explained by the failure of the peak assumption at such masses, an issue unrelated to the choice of the barrier.
- The PBS using the constant spherical collapse barrier is no better than 10%.

We also provide fitting formulas for b_2 , b_3 as a function of b_1 which are valid over a range of redshifts and can be useful for predictions and forecasts based on halo statistics, such as for example the halo model.

In the future, we plan to extend our analysis to accurately measure assembly bias, i.e. the dependence of bias on halo properties beyond the mass (e.g., [44–46]). Further, it will be interesting to extend this technique beyond the infinite wavelength, spherically symmetric “separate universe” to allow for precision measurements of the tidal and scale-dependent biases.

Acknowledgments

We thank Aseem Paranjape, Marcello Musso and Vincent Desjacques for useful discussion about the ESP. F.S. acknowledges support from the Marie Curie Career Integration

Grant (FP7-PEOPLE-2013-CIG) ‘‘FundPhysicsAndLSS’’. T.B. gratefully acknowledges support from the Institute for Advanced Study through a Corning Glass works foundation grant.

A Halo bias from excursion set peaks

In this appendix, we present details of the derivation of the Lagrangian bias parameters of halos in the ESP formalism. We first introduce some notation, following [19]. The top-hat and Gaussian filters in Fourier space are given by

$$W_{\text{TH}}(kR_{\text{TH}}) = \frac{3}{(kR_{\text{TH}})^3} [\sin(kR_{\text{TH}}) - kR_{\text{TH}}\cos(kR_{\text{TH}})], \quad (\text{A.1})$$

$$W_{\text{G}}(kR_{\text{G}}) = e^{-(kR_{\text{G}})^2/2}, \quad (\text{A.2})$$

respectively. The Gaussian filtered spatial moments are defined as

$$\sigma_{j,\text{G}}^2 \equiv \int d\ln k \Delta^2(k) k^{2j} W_{\text{G}}(kR_{\text{G}})^2, \quad j \geq 1, \quad (\text{A.3})$$

and the first mixed moment as

$$\sigma_{1,\text{m}}^2 \equiv \int d\ln k \Delta^2(k) k^2 W_{\text{G}}(kR_{\text{G}}) W_{\text{TH}}(kR_{\text{TH}}). \quad (\text{A.4})$$

From these quantities we build the characteristic length

$$R_* \equiv \sqrt{3} \frac{\sigma_{1,\text{G}}}{\sigma_{2,\text{G}}}, \quad (\text{A.5})$$

and the spectral moment

$$\gamma \equiv \frac{\sigma_{1,\text{m}}^2}{\sigma_0 \sigma_{2,\text{G}}}. \quad (\text{A.6})$$

Let us begin with Gaussian peaks. Ref. [29] showed that the density of peaks of scaled height ν of a Gaussian-filtered Gaussian random field is

$$n_{\text{pk}}(\nu) = \int dx n_{\text{pk}}(\nu, x) = \frac{e^{-\nu^2/2}}{\sqrt{2\pi}} \frac{G_0(\gamma, \gamma\nu)}{(2\pi R_*^2)^{3/2}}, \quad (\text{A.7})$$

where $x = -\nabla^2\delta/\sigma_2$ is related to the curvature of the field and

$$G_\alpha(\gamma, x_*) \equiv \int dx x^\alpha F(x) p_{\text{G}}(x - x_*; 1 - \gamma^2), \quad (\text{A.8})$$

where $p_{\text{G}}(x - \mu; \sigma^2)$ is a Gaussian distribution with mean μ and variance σ^2 and $F(x)$ is the peak curvature function (Eq. (A15) of BBKS). Notice that in the particular case of a Gaussian filter $R_{\text{G}}\nabla^2\delta = \partial\delta/\partial R_{\text{G}}$ so that x is associated with the curvature of the density field as well as its derivative with respect to the smoothing scale. In the original peak model [29], the smoothing scale R as well as threshold B are fixed, and the peak density is a local function of the smoothed density field ν and its derivatives. On the other hand, in the excursion set, ν is defined at a fixed location, and varies as a function of the smoothing scale. Hence one must be careful when combining the two.

We now apply the excursion set argument on the peaks: on a given smoothing scale σ_0 we consider only the peaks that have a smaller height at an infinitesimally larger smoothing scale.³ We start with the case of a constant barrier of height δ_c . In this case, we ask that the scaled peak height lies between $\nu = \delta_c/\sigma_0$ and $\nu + (d\nu/d\sigma_0)\Delta\nu$. This leads to

$$n_{\text{ESP}}(\nu) = \frac{1}{\gamma\nu} \int_0^\infty dx x n_{\text{pk}}(\nu, x), \quad (\text{A.9})$$

so that the fraction of mass in peaks of height ν is

$$f_{\text{ESP}}(\nu) = V n_{\text{ESP}}(\nu) = \frac{e^{-\nu^2/2}}{\sqrt{2\pi}} \frac{V}{V_*} \frac{G_1(\gamma, \gamma\nu)}{\gamma\nu}, \quad (\text{A.10})$$

where $V_* = (2\pi R_*)^3/2$ and V is the Lagrangian volume associated to the peak and depends on the filter's shape ($V = 4\pi R_{\text{TH}}^3/3$ for a top-hat filter).

We follow [19], who chose a top-hat filter and improved the model by adding a mass-dependent stochastic scatter to the threshold [see Eq. (2.4)]. The peaks on the other hand are defined using a Gaussian filter (which ensures that the higher moments σ_j^2 , $j > 0$ exist). We thus need a mapping between the Gaussian scale R_G and the top-hat one R_{TH} to ensure that the peaks identified in the Gaussian-filtered density field have density contrast $\delta_{\text{TH}} = \delta_c$ when smoothed with a top-hat filter. Following [19], we do that by requiring $\langle \delta_{\text{TH}} \delta_G \rangle = \langle \delta_{\text{TH}}^2 \rangle$ which leads to $R_G = 0.46 R_{\text{TH}}$ with a mild mass dependence that we will not account for.

Including the stochastic parameter β , the fraction of mass corresponding to Eq. (A.10) is now given by

$$f_{\text{ESP}}(\nu) = \int d\beta f_{\text{ESP}}(\nu|\beta) p(\beta), \quad (\text{A.11})$$

where $f_{\text{ESP}}(\nu|\beta)$ is the mass fraction at fixed β and is given by (Eq. (14) of [19])

$$f_{\text{ESP}}(\nu|\beta) = \frac{e^{-(\nu+\beta)^2/2}}{\sqrt{2\pi}} \frac{V}{V_*} \int_{\beta\gamma}^\infty dx \frac{x - \beta\gamma}{\gamma\nu} F(x) p_G(x - \beta\gamma - \gamma\nu; 1 - \gamma^2), \quad (\text{A.12})$$

where $V = 4/3\pi R_{\text{TH}}^3$ is the volume associated with a top-hat filter. Given a probability distribution function (PDF) for β we can thus compute $f_{\text{ESP}}(\nu)$ with Eq. (A.11) and, applying Bayes' theorem, we can compute the PDF for β at fixed ν

$$p(\beta|\nu) = \frac{f_{\text{ESP}}(\nu|\beta) p(\beta)}{f_{\text{ESP}}(\nu)}, \quad (\text{A.13})$$

which we will need to compute the Lagrangian bias parameters.

We can now give predictions for the Lagrangian halo bias, inserting Eq. (A.12) for the multiplicity function into Eq. (2.2). We then apply the PBS argument as described in section 2.1 and send $\nu = \delta_c/\sigma_0$ to $\nu_1 = \nu(1 - \delta_0/\delta_c)$. Notice that the stochastic part of the barrier Eq. (2.4) is not modified. Further, the shift in the barrier (and hence in ν) should not be applied to the denominator of Eq. (A.12) as this factor of ν only appears when one changes variables from $sf(s)$ to $\nu f(\nu)$ and is physically unrelated to the barrier. We then

³This condition is actually not exactly the excursion set condition as expressed by [30]. Indeed we should ask that the peak height be smaller on every smoothing scale larger than σ_0 but this condition is hard to implement. Ref. [47] showed that the much simpler condition that we use here (involving only a single infinitesimally larger smoothing scale), also called up-crossing condition, already gives very accurate predictions.

use Eq. (2.3) to find the bias parameters at fixed β . To obtain the large-scale Lagrangian bias as measured in simulations, one must further marginalize over β . This finally yields

$$\delta_c^n b_n(\nu) = \sum_{i=0}^n \binom{n}{i} \int d\beta p(\beta|\nu) \mu_i(\nu, \beta) \lambda_{n-i}(\nu, \beta), \quad (\text{A.14})$$

with $p(\beta|\nu)$ given by Eq. (A.13) and

$$\begin{aligned} \mu_n(\nu, \beta) &= \nu^n H_n(\nu + \beta), \\ \lambda_n(\nu, \beta) &= (-\Gamma\nu)^n \langle H_n(y - \beta\Gamma - \Gamma\nu) | \nu, \beta \rangle_y, \end{aligned} \quad (\text{A.15})$$

where H_n is the n^{th} order Hermite polynomial, $\Gamma \equiv \gamma/\sqrt{1-\gamma^2}$ and we defined, for any function $h(y, \nu, \beta)$,

$$\langle h(y, \nu, \beta) | \nu, \beta \rangle_y \equiv \frac{\int_{\beta\Gamma}^{\infty} dy (y - \beta\Gamma) F(y\gamma/\Gamma) p_G(y - \beta\Gamma - \Gamma\nu; 1) h(y, \nu, \beta)}{\int_{\beta\Gamma}^{\infty} dy (y - \beta\Gamma) F(y\gamma/\Gamma) p_G(y - \beta\Gamma - \Gamma\nu; 1)}. \quad (\text{A.16})$$

Eq. (A.14) gives the theoretical predictions we compare our results with. This result is the same as the one given in [18, 19] who used

$$\langle 1 + \delta_h | \delta_0, S_0 \rangle \equiv \frac{f(\nu | \delta_0, S_0)}{f(\nu)} = \sum_{n=0}^{\infty} \frac{\delta_0^n b_n}{n!}, \quad (\text{A.17})$$

as the definition of the bias parameters [48, 49], which defines the overdensity of halos δ_h and emphasizes the fact that, in the ESP formalism the effect of the underlying dark matter density field on the abundance of halos of mass M can be estimated from the conditional fraction $f(\nu | \delta_0, S_0)$ of walks that first crossed the barrier of height ν on scale σ_0 having passed through $\delta_0 < B$ on scale $S_0 < \sigma_0$ before.

B Comparison of Lagrangian and Eulerian separate universe biases

To derive the Eulerian bias parameters from the Lagrangian ones, we use the spherical collapse model (which is exact in our case). To do that, we use the result (B.18) of [25] linking $\delta_\rho(t)$ to δ_L . Setting $t = t_0$ (present time) yields $a(t_0) = 1$ which leaves us with

$$\delta_\rho = \sum_{n=1}^{\infty} f_n \delta_L^n, \quad (\text{B.1})$$

with f_n being constant coefficients given in their appendix B. Note that these numbers are derived for a flat matter-dominated (Einstein-de Sitter) universe. However, ref. [25] checked that they are also accurate at the sub-percent level for Λ CDM so that the difference to the exact coefficients for Λ CDM is completely negligible compared to the uncertainties of the measured bias parameters. Then, using the continuity equation for the dark matter density as well as for the density of dark matter halos, the fact that the two comove on large scales, and neglecting δ_ρ at very early times, we find

$$1 + \delta_h = (1 + \delta_\rho) \times (1 + \delta_h^L). \quad (\text{B.2})$$

Finally, we have the bias relations

$$\delta_h^L = \sum_{n=1}^{\infty} \frac{b_n^L}{n!} \delta_L^n, \quad \delta_h = \sum_{n=1}^{\infty} \frac{b_n}{n!} \delta_\rho^n. \quad (\text{B.3})$$

Plugging Eq. (B.1) and Eq. (B.3) into Eq. (B.2), we find

$$b_1 = 1 + b_1^L, \quad (\text{B.4})$$

$$b_2 = \frac{8}{21} b_1^L + b_2^L, \quad (\text{B.5})$$

$$b_3 = -\frac{796}{1323} b_1^L - \frac{13}{7} b_2^L + b_3^L, \quad (\text{B.6})$$

$$b_4 = \frac{476320}{305613} b_1^L + \frac{7220}{1323} b_2^L - \frac{40}{7} b_3^L + b_4^L. \quad (\text{B.7})$$

We can thus compare the Eulerian bias parameters determined from the measured Lagrangian parameters using these relations with the direct Eulerian measurement. This result is shown for b_3 in Figure 5 for a 5th order fit. Clearly, the bias parameters agree very well. This also holds for b_1, b_2 even though we do not show it here. We have found, however, that the polynomial fit is slightly more stable when measuring the Lagrangian bias parameters, i.e. fitting to δ_L rather than δ_ρ . In particular, the covariance between the Eulerian bias parameters b_n and b_{n+1} is reduced when they are derived from the measured Lagrangian bias parameters instead of measuring them directly. This is because the simulated positive and negative values for δ_L are almost symmetric, whereas those for δ_ρ are not due to nonlinear evolution.

C Effect of the degree of the fitting polynomial on the bias parameters

We study here how the degree of the fitting polynomial affects the results. This, along with the covariance between the bias parameters presented in Appendix E, will justify our choice of using a 5th order fit for b_1 to b_3 and a 6th order one for b_4 . We present results for b_3 as this bias parameter is the most sensitive to the degree of the fit, but the effect is qualitatively the same for every bias parameter. Figure 6 shows the results obtained with four different degrees from 3 to 6.

Setting the degree of the fitting polynomial is a balance between a bias in resulting fit parameters (when reducing the polynomial order) and increasing measurement errors (when increasing the order). As Figure 6 shows, we need to go to a 5th order fit in order to have convergence for b_3 (i.e. so that the results obtained with the n^{th} order fit are within the error bars of those obtained with a $n+1$ order polynomial). Hence, to ensure that we obtain unbiased results, we use a 5th order fit to obtain b_1 to b_3 and a 6th order fit for b_4 .

D Fourth order bias

We present here measurements of b_4 that were obtained with a 6th order polynomial fit (Figure 7). The scatter in the points and the uncertainties are quite large for this bias parameter, and only an indication of the general behavior can be seen. For this reason we do not show it in the main text. Nevertheless, the ESP and standard PBS predictions are consistent with the measurements.

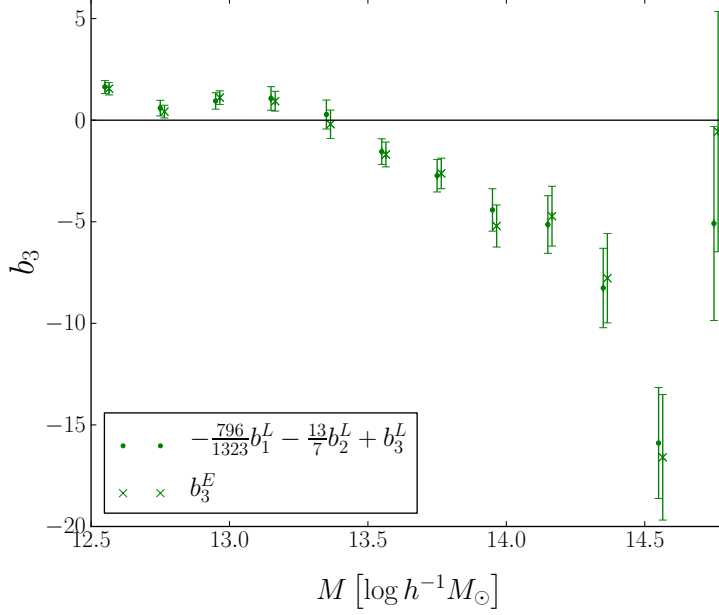


Figure 5: Comparison of b_3 measured directly via fitting δ_h vs the Eulerian density δ_ρ (crosses) and, the corresponding value inferred from the Lagrangian bias fits, as shown in the main text (dots). The crosses have been displaced horizontally for clarity.

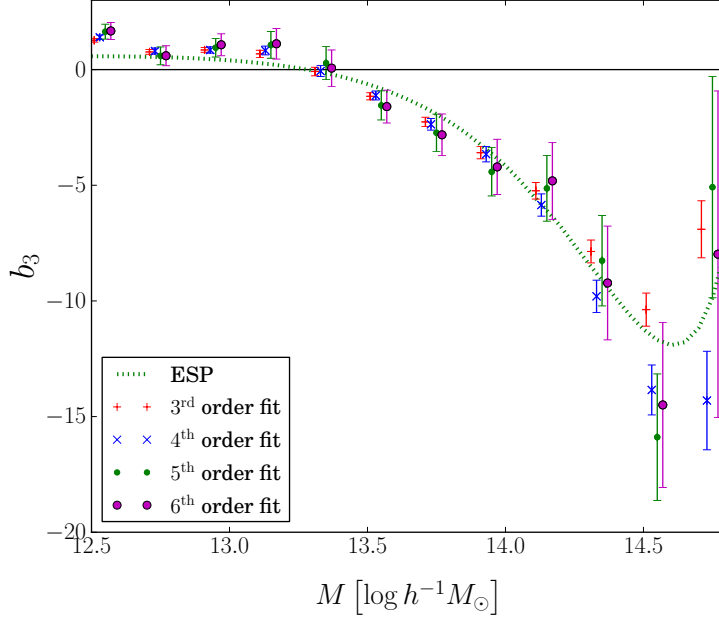


Figure 6: Eulerian b_3 obtained with four different fitting polynomial orders from 3 to 6. For reference, we also show the ESP prediction.

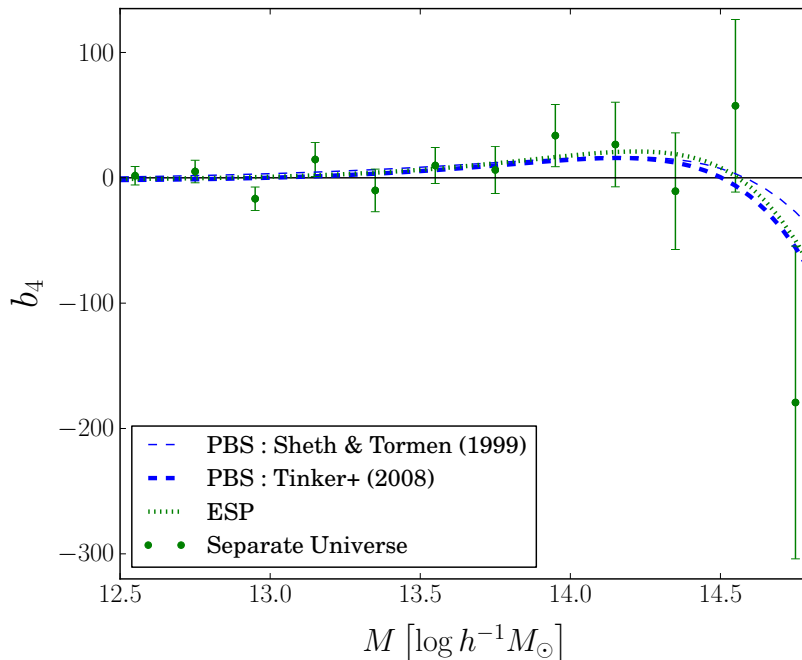


Figure 7: Separate universe results for b_4 . The curves are as in figure 2.

E Covariance between the bias parameters

The bias parameters obtained from separate universe simulations for a given halo sample are in general significantly correlated. From the covariance matrix of the measured Lagrangian bias parameters, we found that b_n^L is correlated with b_{n+2}^L ; this propagates to the Eulerian bias. The correlation coefficients for the Eulerian bias parameters are only weakly dependent on the mass and read $\rho(b_1, b_2) \approx 0.0 \pm 0.15$, $\rho(b_1, b_3) \approx -0.80 \pm 0.05$ and $\rho(b_2, b_3) \approx 0.20 \pm 0.20$ at $z = 0$. Note that the $b_2 - b_3$ correlation is the most mass dependent with $\rho(b_2, b_3) \approx 0$ at low mass and ≈ 0.4 at high mass.

To further illustrate this covariance between the measurements, we show in figure 8 scatter plots of the results obtained with each bootstrap realization in the planes $b_1 - b_2$, $b_1 - b_3$ and $b_2 - b_3$. We present the results at $\log M = 14.15$ and $z = 0$. Each time, we also trace out the contours corresponding to the 68% and 99% confidence levels. The covariance between b_1 and b_3 is clearly significant, illustrating the general trend that b_n is highly correlated with b_{n+2} .

References

- [1] A. Cooray and R. K. Sheth, *Halo models of large scale structure*, *Phys.Rept.* **372** (2002) 1–129, [[astro-ph/0206508](#)].
- [2] J. N. Fry and E. Gaztanaga, *Biasing and hierarchical statistics in large-scale structure*, *Astrophys. J.* **413** (Aug., 1993) 447–452, [[astro-ph/9](#)].
- [3] P. McDonald and A. Roy, *Clustering of dark matter tracers: generalizing bias for the coming era of precision LSS*, *JCAP* **8** (Aug., 2009) 20, [[arXiv:0902.0991](#)].

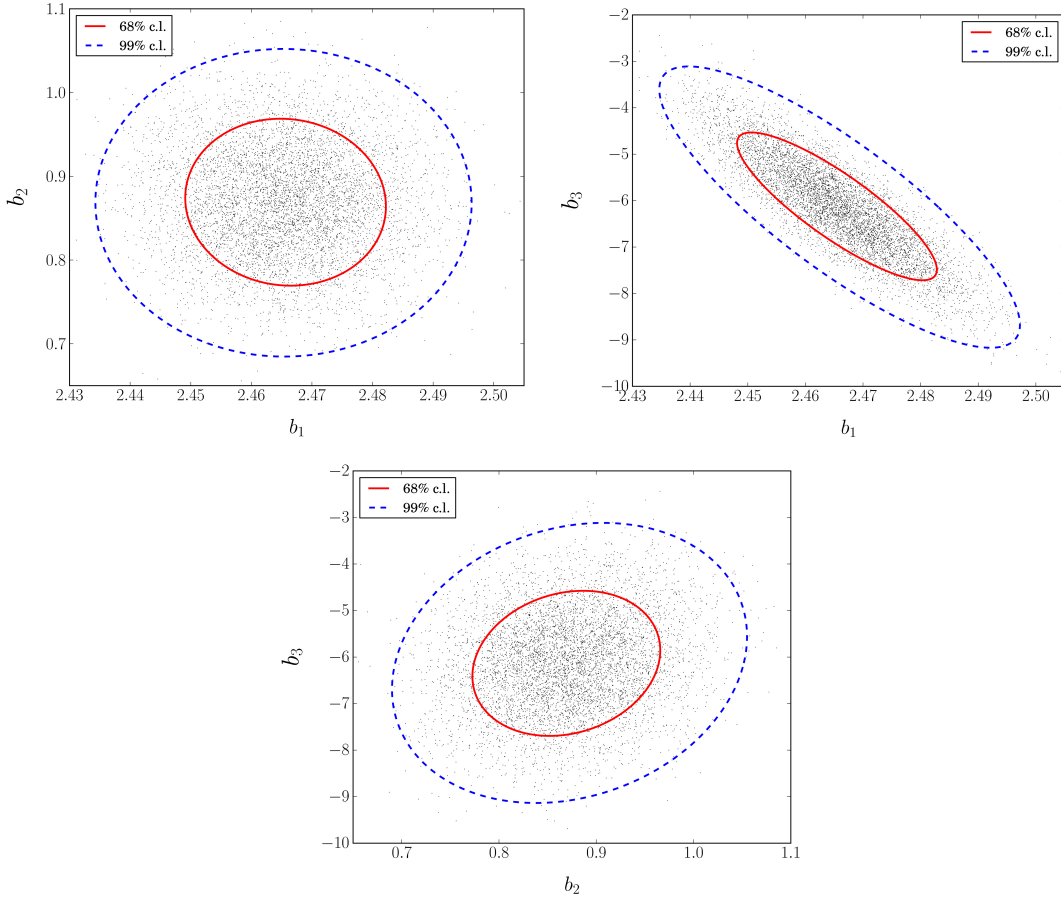


Figure 8: Scatter plots of the results obtained with each bootstrap realization in the planes $b_1 - b_2$, $b_1 - b_3$ and $b_2 - b_3$ at $\log M = 14.15$ and $z = 0$. The contours correspond to 68% (red) and 99% (dashed blue) confidence levels.

- [4] M. Mirbabayi, F. Schmidt, and M. Zaldarriaga, *Biased tracers and time evolution*, *JCAP* **7** (July, 2015) 30, [[arXiv:1412.5169](#)].
- [5] L. Senatore, *Bias in the Effective Field Theory of Large-Scale Structures*, [arXiv:1406.7843](#).
- [6] P. McDonald, *Clustering of dark matter tracers: Renormalizing the bias parameters*, *Phys. Rev. D* **74** (Nov., 2006) 103512, [[astro-ph/0](#)].
- [7] V. Assassi, D. Baumann, D. Green, and M. Zaldarriaga, *Renormalized halo bias*, *JCAP* **8** (Aug., 2014) 56, [[arXiv:1402.5916](#)].
- [8] F. Schmidt, D. Jeong, and V. Desjacques, *Peak-background split, renormalization, and galaxy clustering*, *Phys. Rev. D* **88** (July, 2013) 023515, [[arXiv:1212.0868](#)].
- [9] G. Lemaître, *L'Univers en expansion*, *Annales de la Societe Scientifique de Bruxelles* **53** (1933) 51.
- [10] E. Sirko, *Initial conditions to cosmological N-body simulations, or how to run an ensemble of simulations*, *Astrophys. J.* **634** (2005) 728–743, [[astro-ph/0503106](#)].
- [11] T. Baldauf, U. Seljak, L. Senatore, and M. Zaldarriaga, *Galaxy Bias and non-Linear Structure Formation in General Relativity*, *JCAP* **1110** (2011) 031, [[arXiv:1106.5507](#)].

- [12] Y. Li, W. Hu, and M. Takada, *Super-sample covariance in simulations*, *Phys. Rev. D* **89** (Apr., 2014) 083519, [[arXiv:1401.0385](#)].
- [13] C. Wagner, F. Schmidt, C.-T. Chiang, and E. Komatsu, *Separate Universe Simulations*, *Mon.Not.Roy.Astron.Soc.* **448** (2015) 11, [[arXiv:1409.6294](#)].
- [14] T. Baldauf, U. Seljak, L. Senatore, and M. Zaldarriaga, *Galaxy Bias and non-Linear Structure Formation in General Relativity*, *JCAP* **1110** (2011) 031, [[arXiv:1106.5507](#)].
- [15] D. Jeong, F. Schmidt, and C. M. Hirata, *Large-scale clustering of galaxies in general relativity*, *Phys. Rev. D* **85** (Jan., 2012) 023504, [[arXiv:1107.5427](#)].
- [16] N. Kaiser, *On the spatial correlations of Abell clusters*, *Astrophys. J. Lett.* **284** (Sept., 1984) L9–L12.
- [17] H. J. Mo and S. D. M. White, *An analytic model for the spatial clustering of dark matter haloes*, *MNRAS* **282** (Sept., 1996) 347–361, [[astro-ph/9](#)].
- [18] A. Paranjape and R. K. Sheth, *Peaks theory and the excursion set approach*, *MNRAS* **426** (Nov., 2012) 2789–2796, [[arXiv:1206.3506](#)].
- [19] A. Paranjape, R. K. Sheth, and V. Desjacques, *Excursion set peaks: a self-consistent model of dark halo abundances and clustering*, *MNRAS* **431** (May, 2013) 1503–1512, [[arXiv:1210.1483](#)].
- [20] R. E. Angulo, C. M. Baugh, and C. G. Lacey, *The assembly bias of dark matter haloes to higher orders*, *MNRAS* **387** (June, 2008) 921–932, [[arXiv:0712.2280](#)].
- [21] M. Manera and E. Gaztañaga, *The local bias model in the large-scale halo distribution*, *MNRAS* **415** (July, 2011) 383–398, [[arXiv:0912.0446](#)].
- [22] A. Paranjape, E. Sefusatti, K. C. Chan, V. Desjacques, P. Monaco, and R. K. Sheth, *Bias deconstructed: unravelling the scale dependence of halo bias using real-space measurements*, *MNRAS* **436** (Nov., 2013) 449–459, [[arXiv:1305.5830](#)].
- [23] Y. Li, W. Hu, and M. Takada, *Separate Universe Consistency Relation and Calibration of Halo Bias*, *ArXiv e-prints* (Nov., 2015) [[arXiv:1511.01454](#)].
- [24] T. Baldauf, U. Seljak, L. Senatore, and M. Zaldarriaga, *Linear response to long wavelength fluctuations using curvature simulations*, *ArXiv e-prints* (Nov., 2015) [[arXiv:1511.01465](#)].
- [25] C. Wagner, F. Schmidt, C.-T. Chiang, and E. Komatsu, *The angle-averaged squeezed limit of nonlinear matter N -point functions*, [[arXiv:1503.03487](#)].
- [26] S. Cole and N. Kaiser, *Biased clustering in the cold dark matter cosmogony*, *MNRAS* **237** (Apr., 1989) 1127–1146.
- [27] R. K. Sheth and G. Tormen, *Large scale bias and the peak background split*, *Mon.Not.Roy.Astron.Soc.* **308** (1999) 119, [[astro-ph/9901122](#)].
- [28] J. L. Tinker, A. V. Kravtsov, A. Klypin, K. Abazajian, M. S. Warren, et al., *Toward a halo mass function for precision cosmology: The Limits of universality*, *Astrophys.J.* **688** (2008) 709–728, [[arXiv:0803.2706](#)].
- [29] J. M. Bardeen, J. R. Bond, N. Kaiser, and A. S. Szalay, *The statistics of peaks of Gaussian random fields*, *Astrophys. J.* **304** (May, 1986) 15–61.
- [30] J. Bond, S. Cole, G. Efstathiou, and N. Kaiser, *Excursion set mass functions for hierarchical Gaussian fluctuations*, *Astrophys.J.* **379** (1991) 440.
- [31] B. E. Robertson, A. V. Kravtsov, J. Tinker, and A. R. Zentner, *Collapse Barriers and Halo Abundance: Testing the Excursion Set Ansatz*, *The Astrophysical Journal* **696** (May, 2009) 636–652.
- [32] V. Springel, *The Cosmological simulation code GADGET-2*, *Mon.Not.Roy.Astron.Soc.* **364** (2005) 1105–1134, [[astro-ph/0505010](#)].

- [33] S. P. Gill, A. Knebe, and B. K. Gibson, *The Evolution substructure 1: A New identification method*, *Mon.Not.Roy.Astron.Soc.* **351** (2004) 399, [[astro-ph/0404258](#)].
- [34] S. R. Knollmann and A. Knebe, *Ahf: Amiga’s Halo Finder*, *Astrophys.J.Suppl.* **182** (2009) 608–624, [[arXiv:0904.3662](#)].
- [35] T. Baldauf, U. Seljak, V. Desjacques, and P. McDonald, *Evidence for quadratic tidal tensor bias from the halo bispectrum*, *Phys. Rev. D* **86** (Oct., 2012) 083540, [[arXiv:1201.4827](#)].
- [36] S. Saito, T. Baldauf, Z. Vlah, U. Seljak, T. Okumura, and P. McDonald, *Understanding higher-order nonlocal halo bias at large scales by combining the power spectrum with the bispectrum*, *Phys. Rev.* **D90** (2014), no. 12 123522, [[arXiv:1405.1447](#)].
- [37] M. Schmittfull, T. Baldauf, and U. Seljak, *Near optimal bispectrum estimators for large-scale structure*, *Phys. Rev.* **D91** (2015), no. 4 043530, [[arXiv:1411.6595](#)].
- [38] D. Foreman-Mackey, D. W. Hogg, D. Lang, and J. Goodman, *emcee: The MCMC Hammer*, *Publications of the Astronomical Society of the Pacific* **125** (Mar., 2013) 306–312, [[arXiv:1202.3665](#)].
- [39] J. L. Tinker, B. E. Robertson, A. V. Kravtsov, A. Klypin, M. S. Warren, et al., *The Large Scale Bias of Dark Matter Halos: Numerical Calibration and Model Tests*, *Astrophys.J.* **724** (2010) 878–886, [[arXiv:1001.3162](#)].
- [40] A. D. Ludlow and C. Porciani, *The peaks formalism and the formation of cold dark matter haloes*, *MNRAS* **413** (May, 2011) 1961–1972, [[arXiv:1011.2493](#)].
- [41] M. Musso and R. K. Sheth, *The importance of stepping up in the excursion set approach*, *Mon. Not. Roy. Astron. Soc.* **438** (2014), no. 3 2683–2693, [[arXiv:1306.0551](#)].
- [42] K. Hoffmann, J. Bel, and E. Gaztanaga, *Comparing halo bias from abundance and clustering*, *Mon. Not. Roy. Astron. Soc.* **450** (2015), no. 2 1674–1692, [[arXiv:1503.00313](#)].
- [43] M. Manera, R. K. Sheth, and R. Scoccimarro, *Large-scale bias and the inaccuracy of the peak-background split*, *MNRAS* **402** (Feb., 2010) 589–602, [[arXiv:0906.1314](#)].
- [44] L. Gao, V. Springel, and S. D. M. White, *The Age dependence of halo clustering*, *Mon. Not. Roy. Astron. Soc.* **363** (2005) L66–L70, [[astro-ph/0506510](#)].
- [45] R. H. Wechsler, A. R. Zentner, J. S. Bullock, A. V. Kravtsov, and B. Allgood, *The Dependence of Halo Clustering on Halo Formation History, Concentration, and Occupation*, *Astrophys. J.* **652** (Nov., 2006) 71–84, [[astro-ph/0512416](#)].
- [46] N. Dalal, M. White, J. R. Bond, and A. Shirokov, *Halo Assembly Bias in Hierarchical Structure Formation*, *Astrophys. J.* **687** (Nov., 2008) 12–21, [[arXiv:0803.3453](#)].
- [47] M. Musso and R. K. Sheth, *One step beyond: The excursion set approach with correlated steps*, *Mon.Not.Roy.Astron.Soc.* **423** (2012) L102–L106, [[arXiv:1201.3876](#)].
- [48] H. J. Mo and S. D. M. White, *An Analytic model for the spatial clustering of dark matter halos*, *Mon. Not. Roy. Astron. Soc.* **282** (1996) 347, [[astro-ph/9512127](#)].
- [49] H. J. Mo, Y. P. Jing, and S. D. M. White, *High-order correlations of peaks and halos: A Step toward understanding galaxy biasing*, *Mon. Not. Roy. Astron. Soc.* **284** (1997) 189, [[astro-ph/9603039](#)].